

## Cubic $\text{In}_2\text{O}_3$ Microparticles for Efficient Photoelectrochemical Oxygen Evolution

Ming Meng,<sup>†</sup> Xinglong Wu,<sup>\*,†,‡</sup> Xiaobin Zhu,<sup>†</sup> Lun Yang,<sup>†</sup> Zhixing Gan,<sup>†</sup> Xiaoshu Zhu,<sup>§</sup> Lizhe Liu,<sup>†</sup> and Paul K. Chu<sup>||</sup>

<sup>†</sup>Key Laboratory of Modern Acoustics, MOE, Institute of Acoustics, Collaborative Innovation Center of Advanced Microstructures and Department of Physics, Nanjing University, Nanjing 210093, P. R. China

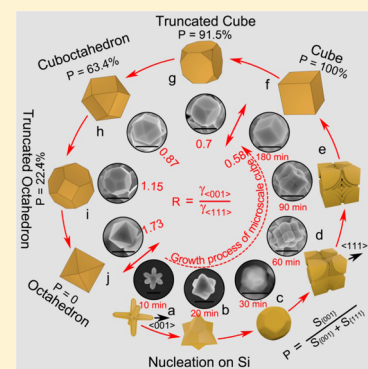
<sup>‡</sup>Department of Physics, NingBo University, NingBo 3153001, China

<sup>§</sup>Center for Analysis and Testing, Nanjing Normal University, Nanjing 210093, P. R. China

<sup>||</sup>Department of Physics and Materials Science, City University of Hong Kong, Tat Chee Avenue, Kowloon, Hong Kong, China

### Supporting Information

**ABSTRACT:** Cubic  $\text{In}_2\text{O}_3$  microparticles with exposed  $\{001\}$  facets as well as single morphology and size are produced on a large scale on silicon with a high yield. The morphological evolution during chemical vapor deposition is investigated and the new knowledge enables precise facet cutting. The synthesized Cubic  $\text{In}_2\text{O}_3$  microparticles possess superior photoelectrocatalytic activity and excellent chemical and structural stability in oxygen evolution reaction on account of the unique surface structure and electronic band structure of the  $\{001\}$  facets. Our results reveal that it is feasible to promote the photoelectrochemical water splitting efficiency of photoanode materials by controlling the growth on specific crystal facets. The technique and concept can be extended to other facet-specific materials in applications such as sensors, solar cells, and lithium batteries.



### SECTION: Surfaces, Interfaces, Porous Materials, and Catalysis

Controlled growth on specific crystal facets of inorganic functional materials has spurred many promising applications in photocatalysis,<sup>1–4</sup> photoelectrochemical (PEC) water splitting,<sup>5</sup> dye-sensitized solar cells,<sup>6</sup> gas sensing,<sup>7</sup> and lithium batteries.<sup>8</sup> Among these applications, PEC water splitting based on oxidation–reduction at the semiconductor/electrolyte interface is of particular interest as it integrates both solar energy collection and  $\text{H}_2/\text{O}_2$  evolution.<sup>9–11</sup> Crystal facets with different atomic arrangements not only offer different active sites to break chemical bonds, but also create different barriers at the semiconductor/electrolyte interface, thereby providing the opportunity to design new materials with enhanced PEC performance.<sup>12,13</sup> It has been shown that photoexcited electrons and holes can gather on different crystal facets leading to increased separation of photogenerated electron/hole pairs.<sup>14–18</sup> This also implies that the exposed crystal facets play an important role in the PEC properties of semiconductor photoelectrodes, and precise control of the crystal facet is crucial.

Indium oxide ( $\text{In}_2\text{O}_3$ ) with a body-center-cube (bcc) structure is an ideal model photocatalyst on account of its proper band-edge position, excellent conductivity, and superior PEC stability.<sup>5,15,19–22</sup> Unique to  $\text{In}_2\text{O}_3$  facets is that polar  $\{001\}$  facets have the capability to dissociate adsorbed  $\text{H}_2\text{O}$  molecules into  $\text{H}^+$  and  $\text{OH}^-$ , whereas nonpolar  $\{111\}$  facets cannot do so.<sup>5,15</sup> This suggests that the photocatalytic activity

can be enhanced appreciably by precise cutting of the specific crystal facets.<sup>23</sup> In addition, our first-principles calculation suggests that a new valence sub-band appears just below and very close to the Fermi level defined as the energy of the highest occupied state set to zero energy according to customary convention because of the cleaving of the  $\{001\}$  facets.<sup>5,15</sup> It is crucial to accumulate the positively charged holes on the  $\{001\}$  facets because the valence sub-band is originally totally filled, and any deviation from this full situation should cause creation of holes. Thus, it is possible that  $\text{In}_2\text{O}_3$  cubes with only the  $\{001\}$  facets exposed possess significantly enhanced PEC water splitting activity. The working principle of this photoanode system is illustrated in Figure 1.  $\text{In}_2\text{O}_3$  cubes absorb photons that cause generation of both valence band holes and conduction band electrons. Energetic electrons flow to the cathode (Pt) via the external circuit and participate in the hydrogen evolution half-reaction, whereas energetic holes accumulate on the  $\{001\}$  facets due to the new valence sub-band, where these holes can transfer to the adsorbed water molecules to produce oxidation reaction. When the adsorbed water molecules are dissociated into  $\text{H}^+$  and  $\text{OH}^-$ , transfer of

Received: November 1, 2014

Accepted: November 30, 2014

Published: November 30, 2014

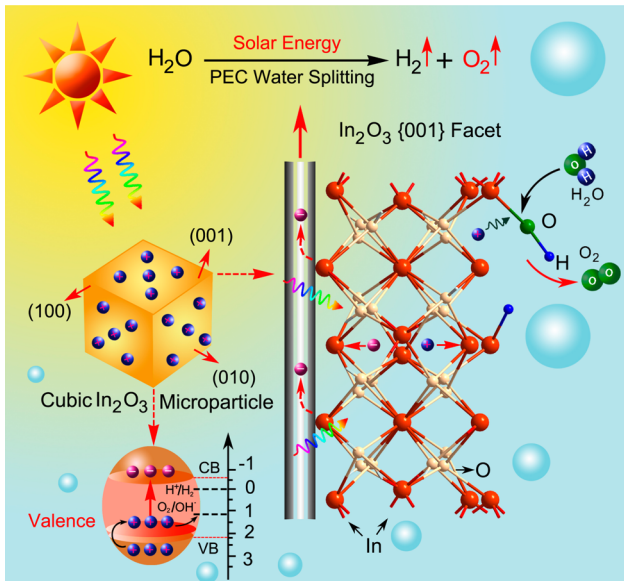


**Figure 1.** Schematic illustration of PEC water splitting on the surface of cubic  $\text{In}_2\text{O}_3$  photoanode. Photogenerated holes migrate to the surface of the cube and react with adsorbed  $\text{H}_2\text{O}$  molecules, which are dissociated into  $\text{H}^+$  and  $\text{OH}^-$  on the  $\{001\}$  facets, subsequently causing oxygen evolution. Here, the big red and small light yellow balls represent In and O atoms in the photoanode, whereas the big green and small blue balls stand for O and H atoms, respectively.

holes is expected to be more efficient because the activation barrier of oxygen evolution is reduced significantly. That is, the photogenerated holes have lower activation barrier to oxidize  $-\text{OH}$  than directly split water. Consequently, the oxygen evolution reaction continues in concert with the sustained dynamic process of  $\text{H}_2\text{O}$  adsorption and dissociation.

Truncated octahedral  $\text{In}_2\text{O}_3$  microcrystals have recently been synthesized.<sup>5</sup> Owing to the presence of the exposed  $\{001\}$

facets, they exhibit higher photoelectrocatalytic activity in comparison with octahedral  $\text{In}_2\text{O}_3$  microcrystals fully enclosed by the  $\{111\}$  facets. Synthesis of cubic  $\text{In}_2\text{O}_3$  microcrystals with the fully exposed  $\{001\}$  facets is thus highly desirable to further improve the photoelectrocatalytic performance. Theoretically, cubic crystal symmetry endows  $\text{In}_2\text{O}_3$  with abundant morphologies.<sup>24,25</sup> Although nanostructured  $\text{In}_2\text{O}_3$  single crystals with a larger percentage of exposed  $\{001\}$  facets have been fabricated,<sup>26–29</sup> the yield tends to be low and size is nonuniform, thereby making it difficult to study the photoactivity of different facets accurately. In addition, most importantly, the underlying mechanism of  $\text{In}_2\text{O}_3$  morphological evolution is not clear, and, in fact, some reports about the effects of the synthesis parameters on morphology evolution are sometimes contradictory.<sup>30,31</sup> In this work, we systematically investigate the morphological evolution mechanism of  $\text{In}_2\text{O}_3$  microcrystals, and with the new understanding, cubic  $\text{In}_2\text{O}_3$  microcrystals with a single morphology and uniform size are produced on a large scale with a high yield by a modified chemical vapor deposition (CVD) method (Figure S1 in Supporting Information). The facet-controlled  $\text{In}_2\text{O}_3$  microcubes show a larger photocurrent density in PEC water splitting than those with a smaller percentage of the exposed  $\{001\}$  facets and the Faraday efficiency of oxygen evolution reaction reaches 91.7%. The results provide evidence about the importance of precise and controlled facet cutting of inorganic microcrystals.

Previous reports have demonstrated that the crystal morphology of a cubic structure is dictated by the ratio ( $R$ ) between the growth rates along the  $\langle 001 \rangle$  and  $\langle 111 \rangle$  directions and intrinsically determined by the surface energy of the facets.<sup>24,32</sup> With regard to the bcc  $\text{In}_2\text{O}_3$ , the sequence of surface-energy ( $\gamma$ ) for low-index crystallographic facets is  $\gamma_{\{111\}} < \gamma_{\{001\}} < \gamma_{\{110\}}$ , and the growth rate of the corresponding facets follow the same sequence.<sup>33</sup> Consequently, altering the relative order of the surface energy is prerequisite to precise control of

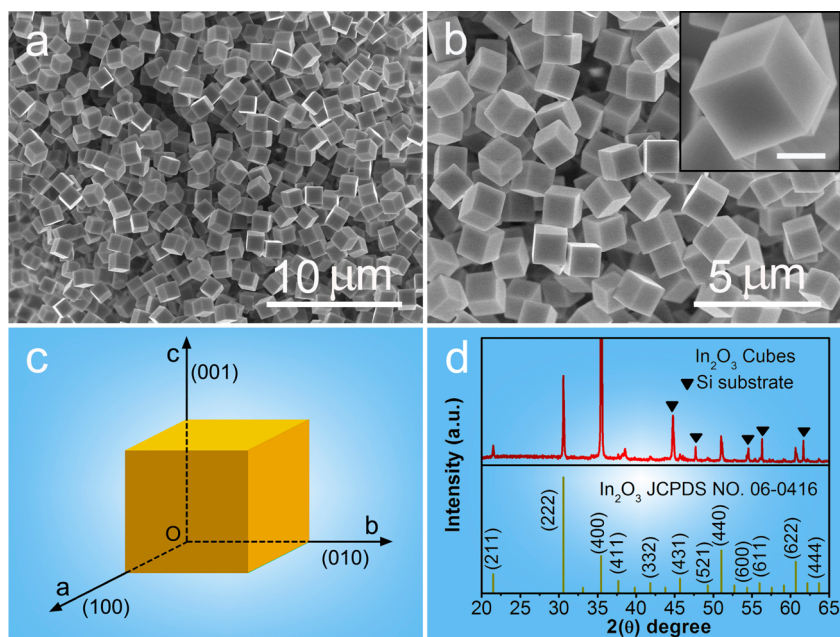


**Figure 2.** (a,b) Low- and high-magnification FE-SEM images of the as-synthesized cubic  $\text{In}_2\text{O}_3$  microparticles on silicon substrate. The inset in panel b shows an enlarged single microcube; scale bar: 500 nm. (c) Schematic diagram of a cubic microcrystal. The six side facets are  $\{001\}$ . (d) Corresponding XRD pattern dominated by high-energy  $\{001\}$  facets. The peaks with labels ( $\blacktriangledown$ ) are from the Si substrate.

the  $\text{In}_2\text{O}_3$  crystal morphology. In the CVD approach, the surface energy sequence can be altered by gas-phase supersaturation related to the growth temperature.<sup>28,34,35</sup>

A large quantity of cubic  $\text{In}_2\text{O}_3$  microcrystals with good uniformity is fabricated by the modified CVD route at 1000 °C based on the carbothermal reduction reaction (Figure S2 in the Supporting Information). Figure 2a shows that the cubic  $\text{In}_2\text{O}_3$  crystals have a narrow size distribution, and the average size is approximately 1  $\mu\text{m}$  (Figure 2b). The inset in Figure 2b shows the magnified field-emission scanning electron microscopy (FE-SEM) image of an individual cube with smooth square facets. The shape is described by the 3D representation in Figure 2c. Figure 2d presents the X-ray diffraction (XRD) pattern of the cubic  $\text{In}_2\text{O}_3$  crystals and standard card (JCPDS card No. 06-416). All the diffraction peaks can be indexed to the bcc structure of  $\text{In}_2\text{O}_3$  (space group  $I_a^3$ ,  $T_h$ ) except those from the silicon substrate (Figure S3 in the Supporting Information). Moreover, the diffraction intensity ratio of the (400) to (222) peak is much larger than that in the standard powder pattern (6.5 versus 0.3), indicating that more {001} facets are exposed. A typical SEM image and schematic model of a cubic microcrystal viewed along the [001] direction are shown in Figures 3a,b, which clearly reveal that the projection is a two-dimensional square constructed by edges of [010] and [100]. This is also verified by the low-magnification transmission electron microscopy (TEM) image (Figure 3c). The selected-area electron diffraction (SAED) pattern with a square symmetry and two sets of square crossing 0.506 nm fringes consistent with the {002} lattice spacing of bcc  $\text{In}_2\text{O}_3$  are

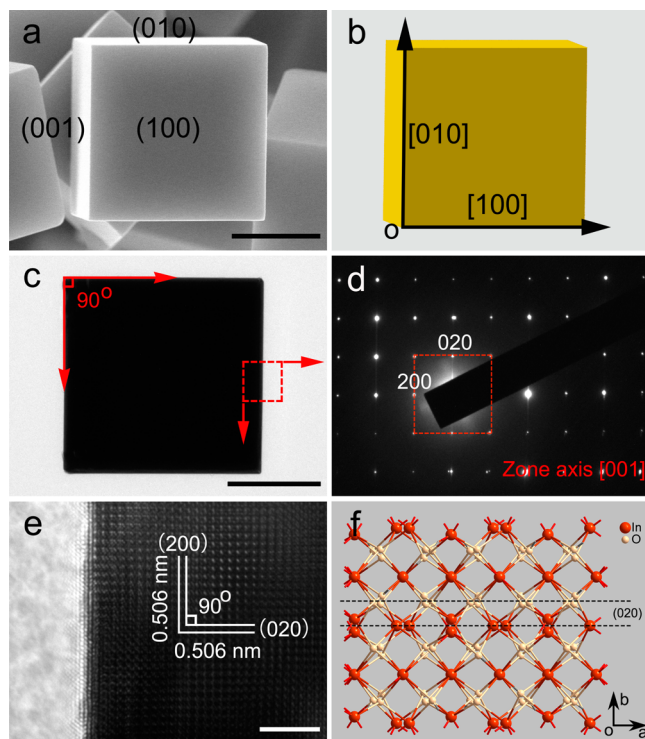


**Figure 3.** (a) SEM image (scale bar: 500 nm) and (b) stimulated image of a cubic crystal viewed along the [001] direction. (c) Typical low-magnification TEM image of a cubic  $\text{In}_2\text{O}_3$  microcrystal viewed along the [001] direction (scale bar: 500 nm). (d) SAED pattern along the [001] direction and (e) HR-TEM image (scale bar: 5 nm). (f) Schematic model of an ideal  $\text{In}_2\text{O}_3$  cube enclosed by the {001} facets, projected along the [001] direction.

acquired from a same location. The results confirm that each freestanding microcrystal is a single crystal (Figure 3d,e). These crystallographic features are identical to the projected structure model of a cubic  $\text{In}_2\text{O}_3$  microcrystal viewed from the [001] crystallographic direction (Figure 3f), providing convincing evidence that each single-crystal  $\text{In}_2\text{O}_3$  cube is enclosed by six {001} facets.

To investigate the influence of the growth temperature on the  $\text{In}_2\text{O}_3$  microcrystal morphology, experiments are also carried out at different temperature between 920 and 980 °C, while keeping the other experimental parameters the same. When the growth temperature is set to 980 °C, uniform truncated cubes are obtained with a high yield (Figure S4a,b in the Supporting Information). The average size is almost the same as that of the cubes. The magnified FE-SEM image shows that the truncated cube is enclosed by six {001} and eight {111} facets. When the temperature is further reduced, the morphology evolves from cuboctahedral to truncated octahedral and finally octahedral with high symmetry (Figure S4c–h in the Supporting Information). That is to say, the area ratio of the {001} to {111} surface decreases gradually as the temperature is decreased. This is further corroborated by XRD (Figure S5 in the Supporting Information). The diffraction intensity ratio of the (400) to (222) peak decreases from 6.5 for cubes to 4.5, 3.8 for truncated cubes and cuboctahedrons, respectively. In addition, the detailed TEM analysis of the truncated cubes and cuboctahedrons provides the same conclusion (Figure S6 in Supporting Information). According to the ultraviolet–visible (UV–vis) diffusive reflectance spectra acquired from the cubes, truncated cubes, and cuboctahedrons, no obvious difference is observed from the absorbance edges, and all the band gaps are estimated to be about 2.78 eV for these polyhedrons (Figure S7 in the Supporting Information).

According to the temperature-dependent vapor pressure profile (Figure S8 in the Supporting Information), it can be deduced that the gas-phase supersaturation of  $\text{In}_2\text{O}_3$  increases gradually with temperature. To determine the relationship between the supersaturation (growth temperature) and relative growth rate of crystal facets, the growth mechanism of the cube is investigated at different stages, and the results are illustrated in Figure 4.

The CVD process of  $\text{In}_2\text{O}_3$  includes two sequential stages: (i) formation of  $\text{In}_2\text{O}_3$  vapor by chemical reactions occurring in the source materials (discussed in detail in the Supporting Information) and (ii) nucleation and growth of  $\text{In}_2\text{O}_3$  nanocrystals on the silicon substrate. In the early stage, supersaturation is low and a large quantity of  $\text{In}_2\text{O}_3$  exhibits the hexapod-like morphology due to the faster growth rate along the ⟨001⟩ direction (Figure 4a,b and Figure S9a,b). Afterward, newly arriving  $\text{In}_2\text{O}_3$  clusters adsorb on the surface. They are not immediately incorporated into the crystal lattice but are able to diffuse on the surface. In this process, the surface diffusion rate of newly arriving clusters is determined by supersaturation.<sup>36</sup> As growth proceeds, supersaturation reduces the surface diffusion rate of the adsorbed  $\text{In}_2\text{O}_3$  clusters and probability to migrate to the {001} facets with large surface energies. These hexapod-like nanocrystals have a large density of defects such as kinks, ledges, and steps, and growth on the {001} facets is hindered by the defects. When the growth rate on the {001} direction (defined as  $\gamma_{(001)}$ ) is decreased to some extent and becomes comparable to that on the {111} direction (denoted as  $\gamma_{(111)}$ ), the morphology of the  $\text{In}_2\text{O}_3$  nanocrystal

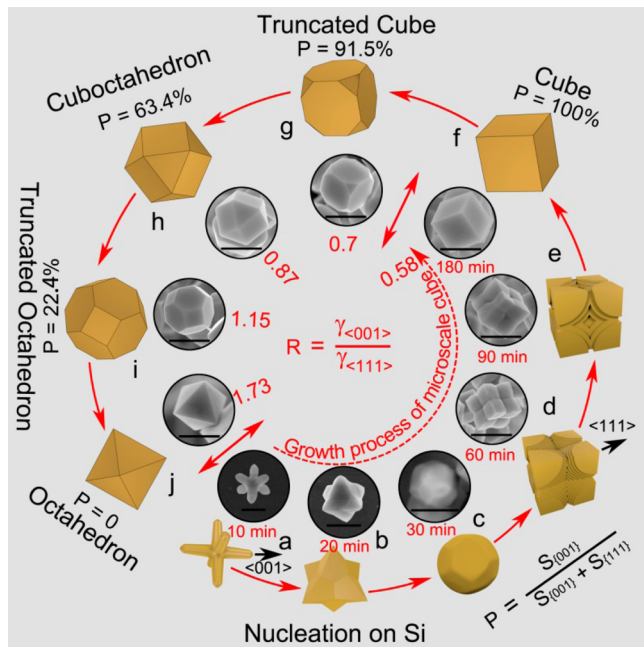


**Figure 4.** Morphological evolution of  $\text{In}_2\text{O}_3$  microcrystals and growth progress of microcubes; scale bar: (a) 50, (b) 300, (c) 500 nm, and (d–j) 1  $\mu\text{m}$ .

changes from hexapod to truncated-octahedron (Figure 4b,c and Figure S9c). With increasing supersaturation,  $\gamma_{\langle 111 \rangle}$  far exceeds  $\gamma_{\langle 001 \rangle}$ , and thus more adsorbed  $\text{In}_2\text{O}_3$  clusters are integrated into the lattice along the  $\langle 111 \rangle$  direction instead of  $\langle 001 \rangle$  as a result of energy conservation (Figure 4d,e).<sup>37</sup> It is

noted that some circular growth steps can be observed from the intermediate product, which stems from growth on the  $\{111\}$  facets (Figure S10 in the Supporting Information). Finally, regular cubes surrounded by smooth  $\{001\}$  facets form (Figure 4f). The observation indicates that the ratio ( $R$ ) between the growth rates along the  $\langle 001 \rangle$  and  $\langle 111 \rangle$  directions decreases with increasing supersaturation. The higher the temperature, the higher the supersaturation, and the high temperature leads to exposure of more high-energy facets. As a result, the ratio ( $R$ ) decreases with increasing temperature. The findings provide the crucial clue in order to understand the temperature-dependent morphological evolution. As the temperature is reduced from 1000 to 920 °C,  $R$  varies from 0.58 to 1.73 resulting in transformation from the cubical to octahedral morphology. This corresponds to gradual reduction of the percentage (defined as  $P$ ) of the exposed  $\{001\}$  facets as shown in Figure 4f–j.

Different gas flow rates lead to different positions of the largest supersaturation in the growth tube and thus drive the morphology evolution of microcrystals at a specific location.<sup>27,34</sup> To demonstrate this effect, more investigation is performed, and it is found that when the flow rate is reduced to 100 sccm (standard-state cubic centimeter per minute), only slightly truncated  $\text{In}_2\text{O}_3$  microcubes are formed under the same other reaction conditions (Figure S11 in the Supporting Information). Since the experiments used to produce these microcubes are performed at a large flow rate of 150 sccm in a small-diameter quartz tube, this results in only slightly different supersaturation along the gas flow direction. Hence, no noticeable morphology change is observed at different flow rates. This reflects that the flow rate is not the main factor here, whereas supersaturation closely related to both the growth

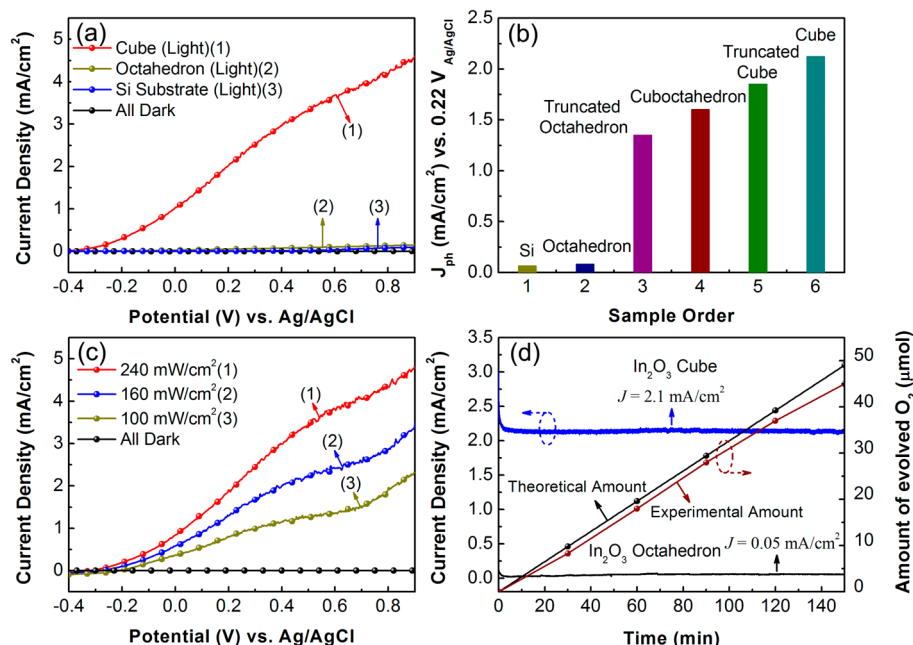


**Figure 5.** (a) Current versus voltage ( $J$ – $V$ ) curves of the polyhedral  $\text{In}_2\text{O}_3$  microparticle photoanodes. The curves are obtained from a 1 M aqueous NaOH (pH = 13.6) solution under illumination (270  $\text{mW}/\text{cm}^2$ ). (b) Comparison of the photocurrent densities ( $0.22 \text{ V}_{\text{Ag}/\text{AgCl}}$ ) of the  $\text{In}_2\text{O}_3$  polyhedrons. (c) Photocurrent density plots of cubic  $\text{In}_2\text{O}_3$  microparticles displaying a photocurrent dependence on illumination power: red (240  $\text{mW}/\text{cm}^2$ ), blue (160  $\text{mW}/\text{cm}^2$ ), pale yellow (100  $\text{mW}/\text{cm}^2$ ). (d) Photocurrent versus time ( $I$ – $t$ ) curves of the  $\text{In}_2\text{O}_3$  microcrystal photoanodes performed at 0.22  $\text{V}_{\text{Ag}/\text{AgCl}}$ . Two sloping curves show the amounts of evolved  $\text{O}_2$  calculated theoretically and detected experimentally of microcube photoelectrode, respectively; Different scales (left axis for the  $I$ – $t$  curves and right axis for the oxygen evolution curves) are used to elucidate the chemical and structural stabilities.

temperature and tube diameter is the primary driving force of the crystal morphology evolution. This is also the reason why we can obtain uniform microcubes at 1000 °C.

To evaluate the PEC water splitting properties of the  $\text{In}_2\text{O}_3$  cubes, photoelectrocatalytic tests are conducted in a deaerated (purified with high purity  $\text{N}_2$  (99.9995%)) three-electrode configuration (Figure S12 in the Supporting Information) employing an epoxy-sealed  $\text{In}_2\text{O}_3$  microcrystal sample as the working electrode with an exposed area of  $0.8 \text{ cm}^2$ , Pt mesh as the counter electrode,  $\text{Ag}/\text{AgCl}$  (3 mol  $\text{L}^{-1}$   $\text{KCl}$ -filled) as a reference electrode, and 1 M  $\text{NaOH}$  ( $\text{pH} = 13.6$ ) solution as the electrolyte. Figure 5a and Figure S13 in the Supporting Information display the current versus voltage ( $J-V$ ) curves of the  $\text{In}_2\text{O}_3$  cubes (red), truncated cubes (gray), cuboctahedrons (green), truncated cuboctahedrons (purple), octahedrons (pale yellow), and blank Si substrate (blue) under light illumination and dark conditions. All the samples exhibit an almost negligible dark current density in a potential range of  $-0.4$  to  $0.9 \text{ V}$  vs  $\text{Ag}/\text{AgCl}$ , suggesting that the observed current stems from light absorption. Under irradiation of a Xe lamp, the photocurrent densities of the  $\text{In}_2\text{O}_3$  cubes, truncated cubes, cuboctahedron and truncated octahedron increase sharply over the entire potential range, and no noticeable photocurrent is observed from the  $\text{In}_2\text{O}_3$  octahedrons and Si substrate, indicating that the photoelectrocatalytic activity is improved largely on the exposed  $\{001\}$  facets. To further investigate the photoelectrocatalytic improvement, the photocurrent densities obtained at  $0.22 \text{ V}$  vs  $\text{Ag}/\text{AgCl}$  [ $1.23 \text{ V}$  vs RHE (reversible hydrogen electrode)] are listed in Figure 5b. At  $0.22 \text{ V}$  vs  $\text{Ag}/\text{AgCl}$ , the current densities of the polyhedrons increase from octahedrons to cubes. The  $\text{In}_2\text{O}_3$  cubes yield a maximal photocurrent density of  $2.1 \text{ mA/cm}^2$ , and it is 42 times the value obtained from  $\text{In}_2\text{O}_3$  octahedrons and much larger than the photocurrent density of  $1.4 \text{ mA/cm}^2$  collected from the  $\text{In}_2\text{O}_3$  truncated octahedrons.<sup>5</sup> This demonstrates that the photocurrent in the process of PEC water splitting is proportional to the percentage of the exposed  $\{001\}$  facets among all the exposed facets.

To further identify the origin of the photocurrent, the power- and wavelength-dependent photocurrent responses are examined. The photocurrent density of the  $\text{In}_2\text{O}_3$  cubes increases with input light power because of more absorbed photons (Figure 5c). Under irradiation by UV-blue light, the  $\text{In}_2\text{O}_3$  cubes/Si substrate shows a large photocurrent response, but the response is reduced largely when irradiated with  $500-700 \text{ nm}$  light (Figure S14a-b). Since the photoexcited electron-hole pairs can still be produced by  $500-700 \text{ nm}$  irradiation for the Si substrate, the enhanced photocurrent response is not due to the Si substrate. In addition, the charge transport across the Si substrate/ $\text{In}_2\text{O}_3$  junction is examined using the  $J-V$  characteristics, and a similar conclusion is obtained (Figure S14c). PEC water splitting performance can also be influenced by the resistivity of the sample, and a lower resistivity usually leads to a larger photocurrent density. However, in the present case, the resistivity of the  $\text{In}_2\text{O}_3$  cubes is  $1.5 \Omega\cdot\text{cm}$ , which is larger than that of  $\text{In}_2\text{O}_3$  truncated octahedrons ( $0.58 \Omega\cdot\text{cm}$ ) and octahedrons ( $0.35 \Omega\cdot\text{cm}$ ).<sup>5</sup> In addition, the nearly identical absorption features in all the polyhedral samples indicate that the enhanced oxygen evolution reaction (OER) of the  $\text{In}_2\text{O}_3$  microcubes cannot be ascribed to improved solar light harvesting due to narrowing of the band gap caused by oxygen vacancies, as reported by previous investigations.<sup>19,20</sup> The above results imply that the superior photoelectrocatalytic

performance of the cubic microcrystals is not due to modification of both the resistivity and absorption feature, but instead the surface structure. The electrochemical impedance spectroscopy data also show clearly that the  $\text{In}_2\text{O}_3$  cubes possess a much lower hole transfer resistance from the surface than octahedrons, thus suggesting the existence of a surface state at the  $\text{In}_2\text{O}_3$   $\{001\}$  facet where holes gather (Figure S15 in the Supporting Information).<sup>38-40</sup> In other words, the exposed  $\{001\}$  facets play a decisive role in the enhanced photoelectrocatalytic activity. It is evident that the  $\{001\}$  facets of  $\text{In}_2\text{O}_3$  possess far better photoelectrocatalytic properties than the  $\{111\}$  facets.

The chemical and structural stability against anodic photo-oxidation is important to photoanode materials. Figure 5d displays the photocurrent-time ( $I-t$ ) curves of  $\text{In}_2\text{O}_3$  microcrystals at a constant potential of  $0.22 \text{ V}$  vs  $\text{Ag}/\text{AgCl}$  under illumination for 150 min. The photocurrent density is very stable, and there is no sign of deterioration in the photocurrent during the entirely measured 20 h (Figure S16a in the Supporting Information). To determine whether the photocurrent stems from the OER on the  $\text{In}_2\text{O}_3$  cube-based photoanode, the amount of oxygen evolved from the photoanode is quantified by a fluorescence sensor and calculated from the  $I-t$  curve assuming 100% Faradaic efficiency (Figure 5d). The amount of evolved oxygen increases linearly with illumination time, suggesting that oxygen evolution is persistent during the entire 150 min of PEC water splitting, and the Faraday efficiency of OER is 91.7%. The 8.3% loss in the Faraday efficiency at 150 min may be due to gas leakage (Figure S16b in the Supporting Information), which can be improved by a better design of the gas test system.<sup>41</sup> Figure S17 shows the SEM and XRD patterns of the  $\text{In}_2\text{O}_3$  cube-based photoanode after water splitting for 150 min. The surface morphology and crystal phase of the  $\text{In}_2\text{O}_3$  cubes remain stable, suggesting that the cubic  $\text{In}_2\text{O}_3$  photoanode has high stability in OER. Our results show that the good PEC water splitting characteristics rendered by the  $\text{In}_2\text{O}_3$  cubes are due to a precise facet.

In conclusion,  $\text{In}_2\text{O}_3$  cubes with exposed  $\{001\}$  facets as well as single morphology and size are produced on a large scale on silicon with a high yield. The morphological evolution during CVD is investigated, and the new knowledge enables precise facet cutting. The synthesized  $\text{In}_2\text{O}_3$  cubes possess superior PEC activity and excellent chemical and structural stability in OER on account of the unique surface structure and electronic band structure of the  $\{001\}$  facets. Our results reveal that it is feasible to promote the PEC water splitting efficiency of photoanode materials by controlling the growth on specific crystal facets. The technique and concept can be extended to other facet-specific materials in applications such as sensors, solar cells, and lithium batteries.

## ASSOCIATED CONTENT

### Supporting Information

Experimental methods, SEM images, TEM and SAED, XRD patterns, and UV/vis absorption spectra of  $\text{In}_2\text{O}_3$  microcrystals with various morphologies, schematic of three-electrode electrochemical cell and experimental apparatus, pressure curves as a function of temperature for  $\text{In}_2\text{O}_3$  crystal, and stability measurement for continuous 20 h. This material is available free of charge via the Internet at <http://pubs.acs.org>.

## AUTHOR INFORMATION

### Corresponding Author

\*E-mail: hklwu@nju.edu.cn.

### Notes

The authors declare no competing financial interest.

## ACKNOWLEDGMENTS

This work was jointly supported by National Basic Research Programs of China under Grant Nos. 2011CB922102, 2013CB932901, and the National Natural Science Foundation (Nos. 11404162 and 11374141). Partial support was also from PAPD, the Research Innovation Program for College Graduates of Jiangsu Province (KYLX-0027), and the City University of Hong Kong Applied Research Grant (ARG) No. 9667085.

## REFERENCES

- (1) Yang, P. D. Crystal Cuts on the Nanoscale. *Nature* **2011**, *482*, 41–42.
- (2) Huang, W. C.; Lyu, L. M.; Yang, Y. C.; Huang, M. H. Synthesis of Cu<sub>2</sub>O Nanocrystals from Cubic to Rhombic Dodecahedral Structures and Their Comparative Photocatalytic Activity. *J. Am. Chem. Soc.* **2012**, *134*, 1261–1267.
- (3) Yang, H. G.; Sun, C. H.; Qiao, S. Z.; Zou, J.; Liu, G.; Smith, S. C.; Cheng, H. M.; Lu, G. Q. Anatase TiO<sub>2</sub> Single Crystals with a Large Percentage of Reactive Facets. *Nature* **2008**, *453*, 638–642.
- (4) Pan, J.; Liu, G.; Lu, G. Q.; Cheng, H. M. On the True Photoreactivity Order of {001}, {010}, and {101} Facets of Anatase TiO<sub>2</sub> Crystals. *Angew. Chem., Int. Ed.* **2011**, *50*, 2133–2137.
- (5) Sun, M.; Xiong, S. J.; Wu, X. L.; He, C. Y.; Li, T. H.; Chu, P. K. Enhanced Photocatalytic Oxygen Evolution by Crystal Cutting. *Adv. Mater.* **2013**, *25*, 2035–2039.
- (6) Hao, F.; Wang, X.; Zhou, C.; Jiao, X. J.; Li, X.; Li, J. B.; Lin, H. Efficient Light Harvesting and Charge Collection of Dye-Sensitized Solar Cells with (001) Faceted Single Crystalline Anatase Nanoparticles. *J. Phys. Chem. C* **2012**, *116*, 19164–19172.
- (7) Han, X. G.; Jin, M. S.; Xie, S. F.; Kuang, Q.; Jiang, Z. Y.; Jiang, Y. Q.; Xie, Z. X.; Zheng, L. S. Synthesis of Tin Dioxide Octahedral Nanoparticles with Exposed High-Energy {221} Facets and Enhanced Gas-Sensing Properties. *Angew. Chem., Int. Ed.* **2009**, *121*, 9344–9347.
- (8) Xiao, X. L.; Liu, X. F.; Zhao, H.; Chen, D. F.; Liu, F. Z.; Xiang, J. H.; Hu, Z. B.; Li, Y. D. Facile Shape Control of Co<sub>3</sub>O<sub>4</sub> and the Effect of the Crystal Plane on Electrochemical Performance. *Adv. Mater.* **2012**, *24*, 5762–5766.
- (9) Linic, S.; Christopher, P.; Ingram, D. B. Plasmonic-Metal Nanostructures for Efficient Conversion of Solar to Chemical Energy. *Nat. Mater.* **2011**, *10*, 911–921.
- (10) Li, Y. F.; Liu, Z. P.; Liu, L. L.; Gao, W. G. Mechanism and Activity of Photocatalytic Oxygen Evolution on Titania Anatase in Aqueous Surroundings. *J. Am. Chem. Soc.* **2010**, *132*, 13008–13015.
- (11) Morales-Guio, C. G.; Tilley, S. D.; Vrubel, H.; Grätze, M.; Hu, X. L. Hydrogen Evolution from a Copper(I) Oxide Photocathode Coated with an Amorphous Molybdenum Sulphide Catalyst. *Nat. Commun.* **2014**, *5*, 3059.
- (12) Choi, K. S. Shape Effect and Shape Control of Polycrystalline Semiconductor Electrodes for Use in Photoelectrochemical Cells. *J. Phys. Chem. Lett.* **2010**, *1*, 2244–2250.
- (13) Tian, N.; Zhou, Z. Y.; Sun, S. G.; Ding, Y.; Wang, Z. L. Synthesis of Tetrahexahedral Platinum Nanocrystals with High-Index Facets and High Electro-Oxidation Activity. *Science* **2007**, *316*, 732–735.
- (14) Li, R. G.; Zhang, F. X.; Wang, D. G.; Yang, J. X.; Li, M. R.; Zhu, J.; Zhou, X.; Han, H. X.; Li, C. Spatial Separation of Photogenerated Electrons and Holes among {010} and {110} Crystal Facets of BiVO<sub>4</sub>. *Nat. Commun.* **2013**, *4*, 1432.
- (15) Meng, M.; Wu, X. L.; Zhu, X. B.; Zhu, X. S.; Chu, P. K. Facet Cutting and Hydrogenation of In<sub>2</sub>O<sub>3</sub> Nanowires for Enhanced Photoelectrochemical Water Splitting. *ACS Appl. Mater. Interfaces* **2014**, *6*, 4081–4088.
- (16) Xing, M. Y.; Yang, B. X.; Yu, H.; Tian, B. Z.; Bagwasi, S.; Zhang, J. L. Enhanced Photocatalysis by Au Nanoparticle Loading on TiO<sub>2</sub> Single-Crystal (001) and (110) Facets. *J. Phys. Chem. Lett.* **2013**, *4*, 3910–3917.
- (17) Tachikawa, T.; Yamashita, S.; Majima, T. Evidence for Crystallite-Face-Dependent TiO<sub>2</sub> Photocatalysis from Single-Molecule Imaging and Kinetic Analysis. *J. Am. Chem. Soc.* **2011**, *133*, 7197–7204.
- (18) Li, R. G.; Han, H. X.; Zhang, F. X.; Wang, D. G.; Li, C. Highly Efficient Photocatalysts Constructed by Rational Assembly of Dual-catalysts Separately on Different Facets of BiVO<sub>4</sub>. *Energy Environ. Sci.* **2014**, *7*, 1369–1376.
- (19) Lei, F. C.; Sun, Y. F.; Liu, K.; Gao, S.; Liang, L.; Pan, B. C.; Xie, Y. Oxygen Vacancies Confined in Ultrathin Indium Oxide Porous Sheets for Promoted Visible-Light Water Splitting. *J. Am. Chem. Soc.* **2014**, *136*, 6826–6829.
- (20) Gan, J. Y.; Lu, X. H.; Wu, J. H.; Xie, S. L.; Zhai, T.; Yu, M. H.; Zhang, Z. S.; Mao, Y. C.; Wang, S. C.; Shen, Y.; Tong, Y. X. Oxygen Vacancies Promoting Photoelectrochemical Performance of In<sub>2</sub>O<sub>3</sub> Nanocubes. *Sci. Rep.* **2013**, *3*, 1021.
- (21) Reyes-Gil, K. R.; Sun, Y. P.; García, E. R.; Raftery, D. Characterization of Photoactive Centers in N-Doped In<sub>2</sub>O<sub>3</sub> Visible Photocatalysts for Water Oxidation. *J. Phys. Chem. C* **2009**, *113*, 12558–12570.
- (22) Reyes-Gil, K. R.; Reyes-García, E. A.; Raftery, D. Nitrogen-Doped In<sub>2</sub>O<sub>3</sub> Thin Film Electrodes for Photocatalytic Water Splitting. *J. Phys. Chem. C* **2007**, *111*, 14579–14588.
- (23) Selloni, A. Anatase Shows Its Reactive Side. *Nat. Mater.* **2008**, *7*, 613–615.
- (24) Wang, Z. L. Transmission Electron Microscopy of Shape-Controlled Nanocrystals and Their Assemblies. *J. Phys. Chem. B* **2000**, *104*, 1153–1175.
- (25) Teo, J. J.; Chang, Y.; Zeng, H. C. Fabrications of Hollow Nanocubes of Cu<sub>2</sub>O and Cu via Reductive Self-Assembly of CuO Nanocrystals. *Langmuir* **2006**, *22*, 7369–7377.
- (26) Yin, W. Y.; Cao, M. H.; Luo, S. J.; Hu, C. W.; Wei, B. Q. Controllable Synthesis of Various In<sub>2</sub>O<sub>3</sub> Submicron/Nanostructures Using Chemical Vapor Deposition. *Cryst. Growth Des.* **2009**, *9*, 2371–2178.
- (27) Yan, Y. G.; Zhou, L. X.; Zhang, Y.; Zhang, J.; Hu, S. Q. Large-Scale Synthesis of In<sub>2</sub>O<sub>3</sub> Nanocubes Under Nondynamic Equilibrium Model. *Cryst. Growth Des.* **2008**, *8*, 3285–3289.
- (28) Yu, J. F.; Wang, Y.; Wen, W.; Yang, D. H.; Huang, B.; Li, J. L.; Wu, K. Aluminothermal Reaction Approach for Micro-/Nanofabrications: Syntheses of In<sub>2</sub>O<sub>3</sub> Micro-/Nanostructures and InN Octahedral Nanoshells. *Adv. Mater.* **2010**, *22*, 1479–1483.
- (29) Shi, M. R.; Xu, F.; Yu, K.; Fang, J. H.; Ji, X. M. Evolution in Shapes of a Series of (111)-Based In<sub>2</sub>O<sub>3</sub> Particles. *Appl. Phys. A: Mater. Sci. Process.* **2008**, *90*, 113–117.
- (30) Shi, M. R.; Xu, F.; Yu, K.; Zhu, Z. Q.; Fang, J. H. Controllable Synthesis of In<sub>2</sub>O<sub>3</sub> Nanocubes, Truncated Nanocubes, and Symmetric Multipods. *J. Phys. Chem. C* **2007**, *111*, 16267–16271.
- (31) Hao, Y. F.; Meng, G. W.; Ye, C. H.; Zhang, L. D. Controlled Synthesis of In<sub>2</sub>O<sub>3</sub> Octahedrons and Nanowires. *Crys. Growth Des.* **2004**, *5*, 1617–1621.
- (32) Sun, Y. G.; Xia, Y. N. Shape-Controlled Synthesis of Gold and Silver Nanoparticles. *Science* **2002**, *298*, 2176–2179.
- (33) Hafeez, M.; Zhai, T. Y.; Bhatti, A. S.; Bando, Y.; Golberg, D. Oxygen Vacancy Driven Modulations in In<sub>2</sub>O<sub>3</sub> Pyramidal Beaded Nanowires. *Cryst. Growth Des.* **2012**, *12*, 4935–4943.
- (34) Ye, C. H.; Fang, X. S.; Hao, Y. F.; Teng, X. M.; Zhang, L. D. Zinc Oxide Nanostructures: Morphology Derivation and Evolution. *J. Phys. Chem. B* **2005**, *109*, 19758–19765.
- (35) Chatterji, D.; Vest, R. W. Thermodynamic Properties of the System Indium-Oxygen. *J. Am. Ceram. Soc.* **1972**, *55*, 575–578.
- (36) Hao, Y. F.; Meng, G. W.; Ye, C. H.; Zhang, X. R.; Zhang, L. D. Kinetics-Driven Growth of Orthogonally Branched Single-Crystalline Magnesium Oxide Nanostructures. *J. Phys. Chem. B* **2005**, *109*, 11204–11208.

- (37) Lin, H. X.; Lei, Z. C.; Jiang, Z. Y.; Hou, C. P.; Liu, D. Y.; Xu, M. M.; Tian, Z. Q.; Xie, Z. X. Supersaturation-Dependent Surface Structure Evolution: From Ionic, Molecular to Metallic Micro/Nanocrystals. *J. Am. Chem. Soc.* **2013**, *131*, 9311–9314.
- (38) Klahr, B.; Gimenez, S.; Fabregat-Santiago, F.; Hamann, T.; Bisquert, J. Water Oxidation at Hematite Photoelectrodes: The Role of Surface States. *J. Am. Chem. Soc.* **2012**, *134*, 4294–4302.
- (39) Klahr, B.; Gimenez, S.; Fabregat-Santiago, F.; Hamann, T.; Bisquert, J.; Hamann, T. Photoelectrochemical and Impedance Spectroscopic Investigation of Water Oxidation with “Co–Pi”-Coated Hematite Electrodes. *J. Am. Chem. Soc.* **2012**, *134*, 16693–16700.
- (40) Riha, S. C.; Klahr, B. M.; Tyo, E. C.; Seifert, S.; Vajda, S.; Pellin, M. J.; Hamann, T. W.; Martinson, A. B. F. Atomic Layer Deposition of a Submonolayer Catalyst for the Enhanced Photoelectrochemical Performance of Water Oxidation with Hematite. *ACS Nano* **2013**, *7*, 2396–2405.
- (41) Hou, Y.; Zuo, F.; Dagg, A.; Feng, P. Y. Visible Light-Driven  $\alpha$ - $\text{Fe}_2\text{O}_3$  Nanorod/Graphene/ $\text{BiV}_{1-x}\text{Mo}_x\text{O}_4$  Core/Shell Heterojunction Array for Efficient Photoelectrochemical Water Splitting. *Nano Lett.* **2012**, *12*, 6464–6473.